Click Here for Full Article

The radiative consistency of Atmospheric Infrared Sounder and Moderate Resolution Imaging Spectroradiometer cloud retrievals

Brian H. Kahn,[1] Evan Fishbein,[1] Shaima L. Nasiri,[2] Annmarie Eldering,[1] Eric J. Fetzer,[1] Michael J. Garay,[1,3] and Sung-Yung Lee[1]

[1] The consistency of cloud top temperature (T_C) and effective cloud fraction (f) retrieved by the Atmospheric Infrared Sounder (AIRS)/Advanced Microwave Sounding Unit (AMSU) observation suite and the Moderate Resolution Imaging Spectroradiometer (MODIS) on the EOS-Aqua platform are investigated. Collocated AIRS and MODIS T_C and f are compared via an "effective scene brightness temperature" ($T_{b,e}$). $T_{b,e}$ is calculated with partial field of view (FOV) contributions from T_C and surface temperature (T_S), weighted by f and $1-f$, respectively. AIRS reports up to two cloud layers while MODIS reports up to one. However, MODIS reports T_C, T_S, and f at a higher spatial resolution than AIRS. As a result, pixel-scale comparisons of T_C and f are difficult to interpret, demonstrating the need for alternatives such as $T_{b,e}$. AIRS-MODIS $T_{b,e}$ differences ($\Delta T_{b,e}$) for identical observing scenes are useful as a diagnostic for cloud quantity comparisons. The smallest values of $\Delta T_{b,e}$ are for high and opaque clouds, with increasing scatter in $\Delta T_{b,e}$ for clouds of smaller opacity and lower altitude. A persistent positive bias in $\Delta T_{b,e}$ is observed in warmer and low-latitude scenes, characterized by a mixture of MODIS CO_2 slicing and 11-μm window retrievals. These scenes contain heterogeneous cloud cover, including mixtures of multilayered cloudiness and misplaced MODIS cloud top pressure. The spatial patterns of $\Delta T_{b,e}$ are systematic and do not correlate well with collocated AIRS-MODIS radiance differences, which are more random in nature and smaller in magnitude than $\Delta T_{b,e}$. This suggests that the observed inconsistencies in AIRS and MODIS cloud fields are dominated by retrieval algorithm differences, instead of differences in the observed radiances. The results presented here have implications for the validation of cloudy satellite retrieval algorithms, and use of cloud products in quantitative analyses.

1. Introduction

[2] Improving knowledge of cloud processes and feedbacks, and their coupling to the global circulation, is one of the most important contemporary issues in atmospheric sciences and climate studies [*Houghton et al.*, 2001; *Stephens*, 2005]. A primary reason for the lack of immediate and meaningful advances in cloud-climate research is the large uncertainty associated with taking observations of the atmospheric cloudy state, including cloud identification, and quantification of cloud optical,

microphysical, and bulk properties. Even though satellite remote sensing has provided a global characterization of clouds, different satellite instruments have not produced a consistent picture of cloud fields [e.g., *Rossow et al.*, 1993; *Thomas et al.*, 2004]. Additional measurements from new sensors aboard the A-Train platforms will provide further capabilities [*Stephens et al.*, 2002]. Until there is progress toward reconciling inconsistencies between satellite measurements, and in understanding the information content of the radiances [*Cooper et al.*, 2006], the full potential of satellite radiances will not be realized.

[3] This paper initiates an ongoing discussion on how to reconcile some of the satellite cloud measurements. We restrict our attention to those parameters primarily affecting outgoing infrared (IR) radiation, and to the cloud products derived from the Atmospheric Infrared Sounder (AIRS) [*Aumann et al.*, 2003] and the Moderate Resolution Imaging Spectroradiometer (MODIS) [*King et al.*, 1992]. Both instruments operate on the Aqua platform and view the

---

[1]Jet Propulsion Laboratory, Pasadena, California, USA.
[2]Department of Atmospheric Sciences, Texas A&M University, College Station, Texas, USA.
[3]Department of Atmospheric and Oceanic Sciences, University of California at Los Angeles, Los Angeles, California, USA.

Table 1. List of Symbols Used and Their Definitions

Symbol	Meaning
B_v	Planck function
B_v^{-1}	Inverse Planck function
f	Effective cloud fraction
f_A	AIRS f
f_M	MODIS f
Δf	AIRS-MODIS f
I	Observed radiance
P_C	Cloud top pressure (hPa)
T_b	Brightness temperature (K)
T_b^{11}	MODIS T_b at 11 μm (K)
T_b^{960}	AIRS T_b at 960 cm^{-1} (K)
$T_{b,e}$	Effective scene T_b (K)
$T_{b,e}^A$	AIRS effective scene T_b (K)
$T_{b,e}^M$	MODIS effective scene T_b (K)
$\Delta T_{b,e}$	AIRS-MODIS $T_{b,e}$ (K)
T_C	Cloud top temperature (K)
T_A	AIRS T_C (K)
T_M	MODIS T_C (K)
T_S	Surface temperature (K)
ΔT_C	$T_A - T_M$ (K)
τ_{IR}	Infrared optical depth
τ_{VIS}	Visible optical depth
Z_A	AIRS cloud top height (km)
Z_M	MODIS cloud top height (km)
$( )_i$	Layer index

same location on the ground nearly simultaneously. The AIRS and MODIS instruments provide some operational redundancy, such as the independent determination of various cloud properties, which can be used to understand and evaluate the strengths of their different observational and retrieval approaches. When differences in the retrieved geophysical parameters occur, it should be a priority to reconcile these as much as possible to improve algorithm performance. Additionally, instrument intercomparisons are necessary if their data is to be used synergistically so that the complimentary strengths of each instrument are emphasized. For example, higher resolution MODIS data allows AIRS-scale spatial heterogeneity to be addressed leading to potentially improved representation of small-scale features in retrieved cloud quantities [*Rossow*, 1989; *Li et al.*, 2004a].

[4] Both AIRS and MODIS on EOS Aqua retrieve a variety of cloud properties from passive IR measurements including effective cloud fraction (f), cloud top height (Z_C), cloud top temperature (T_C), and effective spectral emissivity and reflectivity (see Table 1 for a list of symbols). Because different observational and retrieval approaches are used, fields of T_C and f from the two instruments could be very different. However, the underlying assumption is that, as long as the instruments are working properly, the observed cloud fields should radiate similarly. As will be shown in section 2, the retrieved fields of cloud properties can, in fact, disagree substantially. Therefore at a very fundamental level, we seek to understand if the observed cloud fields agree at least in a radiative sense.

[5] To address the issue of radiative consistency between AIRS and MODIS cloud retrievals, we combine retrieved cloud properties from AIRS and MODIS to arrive at a single parameter we have termed the "effective scene brightness temperature" ($T_{b,e}$), which facilitates more direct comparison of the cloud radiative properties. This parameter, which

is calculated from T_C, surface temperature (T_S), and f, provides an integrated view of AIRS and MODIS cloud scenes. As described below, $T_{b,e}$ is derived by summing the contributions of the fractional cloudy and clear-sky areas of a given AIRS or MODIS field of view (FOV). The agreement in $T_{b,e}$ is a necessary, but not a sufficient, condition for individual agreement in AIRS and MODIS T_C and f. We show that $T_{b,e}$ is useful for determining the agreement of T_C and f for a variety of cloud opacity, height, and layering characteristics.

[6] In section 2, the AIRS and MODIS measurement characteristics and cloud products are presented while highlighting some of the differences in the retrieval methodologies. Next, the collocation approach of AIRS and MODIS measurements is discussed and verified. Then, the method of calculating $T_{b,e}$ is described, and $T_{b,e}$ characteristics are compared to individual cloud products. Section 3 illustrates the behavior of $T_{b,e}$ using a small subset of AIRS data. AIRS and MODIS $T_{b,e}$ differences are correlated to observed cloud configurations. Then, we extend the analysis to four additional granules to address the universality in AIRS and MODIS $T_{b,e}$ behavior. In section 4, we conclude and summarize the results.

2. Methodology

2.1. AIRS and MODIS Clouds

[7] AIRS is a thermal IR grating spectrometer operating in tandem with the Advanced Microwave Sounding Unit (AMSU). AIRS observes radiance with 2378 spectral channels ranging from 3.7 to 15.4 μm, has a nominal spectral resolution of $v/\Delta v \approx 1200$, a footprint size of 13.5 km at nadir, scans $\pm$ 48.95° off nadir, and provides 2.916 million AIRS spectra and 324,000 retrievals globally per day [*Aumann et al.*, 2003]. The AIRS L2 operational retrieval system provides cloud top height (Z_A), cloud top temperature (T_A), and effective cloud fraction (f_A) for up to two layers (see *Susskind et al.* [2003, 2006] and *Kahn et al.* [2007] and references therein for a discussion on AIRS operational cloud retrievals). Research efforts are also underway to retrieve cloud properties, including particle size, optical depth, cloud phase, and water path [*DeSouza-Machado et al.*, 2004; *Li et al.*, 2004b; *Wei et al.*, 2004; *Nasiri and Kahn*, 2006; *Yue et al.*, 2007]; particle size and optical depth of coarse mode dust [*Pierangelo et al.*, 2005; *DeSouza-Machado et al.*, 2006]; and distinguish cirrus from dust [*Hong et al.*, 2006].

[8] MODIS measures thermal IR emission and reflected near-IR and visible radiance in 36 bands from 0.415–14.24 μm at a horizontal spatial resolution of 0.25, 0.5, or 1.0 km, depending on the spectral band [*Platnick et al.*, 2003]. In this work, we use the 5-km resolution MODIS operational cloud top temperature (T_M) and effective cloud fraction (f_M) derived from the CO_2 slicing technique for clouds with cloud top pressures (P_C) less than 700 hPa, or an 11-μm window channel technique (T_b^{11}) for P_C greater than 700 hPa [*Platnick et al.*, 2003]. At least 4 of 25 of 1-km pixels within a 5 $\times$ 5 array must be identified as cloudy according to the cloud mask [*Ackerman et al.*, 1998] in order to attempt the T_b^{11} retrieval [*Menzel et al.*, 2002]. Both T_M and f_M are frequently used as a basis for additional cloud property retrievals. Therefore errors in T_M and f_M impact the
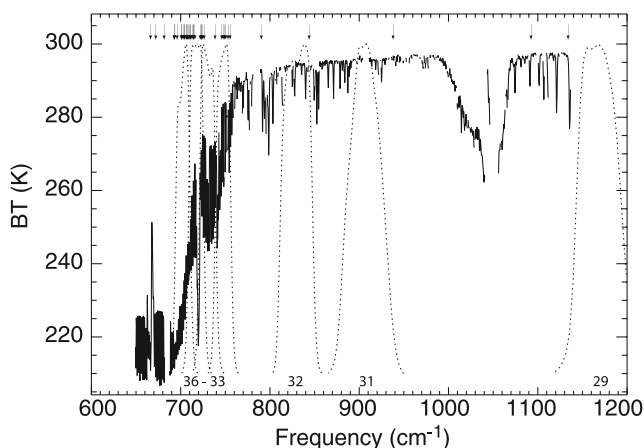
Figure 1. Shown is a representative version 4 cloud-cleared AIRS spectrum from granule 11 (0105 UTC) on 6 September 2002, in the central subtropical Pacific Ocean. The MODIS spectral response functions for selected channels are overlain on the AIRS spectrum, and the channels used for AIRS cloud retrievals are shown with arrows.

retrieval of particle size, optical depth, phase (ice, liquid, or mixed), and water path. This stresses the importance of validating and improving satellite retrievals of T_C and f.

[9] Figure 1 shows the spectral response functions (SRF) of MODIS superimposed over a portion of a representative AIRS spectrum. MODIS channels $32-36$ sense the surface and CO_2, and are used for T_M and f_M retrievals, and channels 29 and 31 sense the surface and H_2O vapor continuum. AIRS uses roughly 50 channels spread over the 15- and 4.2-μm CO_2 bands to detect and locate clouds. In Figure 1, only the channels in the 15-μm band are shown for brevity. As indicated by the figure, AIRS and MODIS T_C and f are derived from similar IR spectral regions (at different spectral resolution) but are based on very different algorithms. The AIRS algorithm uses minimal a priori information, instead relying on a physical retrieval from AMSU radiances that provide estimates of clear-sky radiances, whereas MODIS algorithms use a numerical weather prediction model to provide a priori estimates of clear-sky radiances. The MODIS cloud algorithm operates on 5×5 arrays of MODIS pixels (5 km near nadir resolution) while the AIRS algorithm operates on 3×3 arrays of AIRS footprints (45 km near nadir resolution). The MODIS algorithm averages the pixels in the 5×5 array that are identified as cloudy or probably cloudy by the cloud mask [*Menzel et al.*, 2002] when CO_2 slicing is attempted. When T_b^{11} is used, all pixels are averaged in a 5×5 array in MODIS Collection 4 data.

[10] The AIRS cloud-clearing algorithm estimates clear-sky radiances in the presence of cloudiness using the horizontal heterogeneity within the 3×3 AIRS array. The cloud-cleared radiances are then used to derive the core sounding products of temperature, water vapor, and minor gas profiles. The cloud products T_C and f are derived at the end of the retrieval process from differences in observed and predicted clear-sky radiances. Both AIRS and MODIS cloud property retrievals assume that clouds are opaque with near unity emissivity, but AIRS retrieves up

to two cloud layers per retrieval, while MODIS allows for only a single layer of cloud. Previously, *Rossow et al.* [1985] and *Wielicki and Parker* [1992] showed that different retrieval approaches for identical radiance measurements lead to discrepancies in retrieved cloud quantities. As we show below, discrepancies in AIRS and MODIS cloud quantities do arise not only from the fundamentally different radiance measurements, but more so from the fundamentally different retrieval methodologies, demonstrated by differences in AIRS and MODIS $T_{b,e}$.

2.2. Collocating AIRS and MODIS Clouds

[11] Comparing retrievals of cloud top height (Z_C), cloud top temperature (T_C), and effective cloud fraction (f) from different measurement systems is challenging. Coincident cloud measurements disagree for numerous reasons beyond algorithm-related differences, as described above. The heterogeneity of cloud physical properties over spatial and temporal scales is arguably a principal cause for such disagreements, especially for comparisons involving time-integrated point (for example, surface-based) or line (for example, aircraft) measurements with satellite pixel-level measurements [*Kahn et al.*, 2005, 2007]. In the case of two or more independent satellite measurements, an appropriate and accurate collocation method must be used [e.g., *Li et al.*, 2004a; *Tobin et al.*, 2006]. Furthermore, the geolocation of satellite observations has some inherent error [*Gregorich and Aumann*, 2003], and the spatial response function is not necessarily uniform within a FOV, nor is the contributing radiance necessarily confined within a single FOV [*Cracknell*, 1998]. For example, the AIRS detectors are not perfectly aligned, thus different bandpasses see slightly different FOVs [*Lambrigtsen and Lee*, 2003]. As a result, some AIRS spectra contain discontinuities in radiances that increase in magnitude with increasing cloud heterogeneity [e.g., *Kahn et al.*, 2003, Figure 2]. Even a "perfect" coregistration method that uses an exact spatial response function will be inaccurate to some degree because of geolocation uncertainties.

[12] To demonstrate the accuracy of the collocation methodology, we use AIRS granule number 11 on 6 September 2002, located in the subtropical Pacific Ocean in the Northern Hemisphere, as an illustrative example (Figure 2). (One AIRS granule = 6 min of data, or 90 AIRS footprints per scan line $\times$ 135 scan lines = 12,150 AIRS footprints, and 30 AMSU footprints per scan line $\times$ 45 scan lines = 1350 AMSU footprints.) The dominant dynamical feature is Typhoon Ele, surrounded by a wide variety of cloud types and clear sky, shown with the AIRS brightness temperature at 960 cm^{-1} (T_b^{960}) (Figure 2a). In Figure 2b, we show $\Delta T_b \equiv T_b^{AIRS} - T_b^{MODIS}$ for collocated observations equivalent to MODIS channel 31. ΔT_b is within ~1 K, except for within some of the cloud fields, with the biggest differences (± 5 K) along cloud edges at off-nadir scan angles. Essentially this figure shows the constraints on the "accuracy" of the collocation approach. According to *Tobin et al.* [2006], AIRS and MODIS observed radiances in homogeneous scenes have been shown to agree to within 1.0 K for most MODIS bands, and to 0.1 K for a subset that includes MODIS channel 31. Thus the differences in ΔT_b shown in Figure 2b are primarily a result of imperfect collocation between the AIRS and MODIS observations.
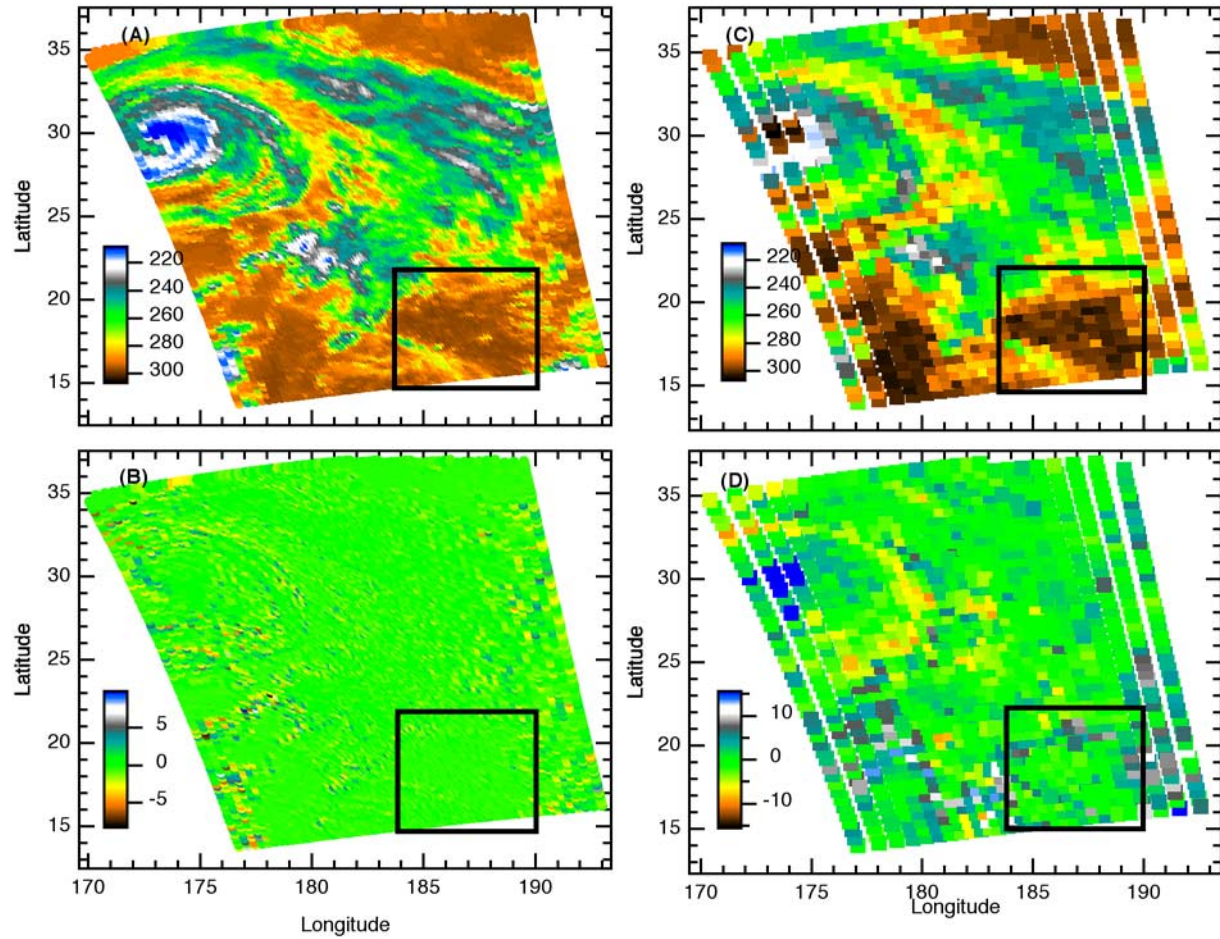
Figure 2. (a) AIRS T_b^{960} (K) for the same granule in Figure 1. (b) Collocated ΔT_b for AIRS and MODIS for an equivalent of MODIS channel 31 (11 μm). (c) $T_{b,e}^A$(K). (d) $\Delta T_{b,e}$ (k). The box highlights a region of focus, to be shown in Figures 6 and 7.

A similar pattern would be expected for both T_C and f, since they are derived from the measured radiances, assuming the retrieval algorithms of AIRS and MODIS were identical.

[13] Collocated ΔT_b in Figure 2b requires three processing steps: the application of (1) a method to collocate simultaneous AIRS and MODIS observations, (2) an approach to smooth MODIS radiances to the AIRS FOV, and (3) a spectral averaging of the high-spectral-resolution information from AIRS to the MODIS spectral resolution. In step 1, the AIRS FOV is approximated as a circle (at nadir view) on a spherical Earth and the FOV changes into an elongated ellipse with increasing view angle (see Appendix A for the formulation and limitations of the collocation method). For step 2, centers of MODIS radiances within the AIRS FOV are weighted equally, averaged over the AIRS FOV, and then converted to T_b. To calculate step 3, an approximate method is employed that spectrally averages AIRS radiances to the MODIS spectral resolution. The radiance of each AIRS channel within the envelope of the MODIS SRF for channel 31 (centered near 11 μm) is weighted by the associated value of the MODIS SRF. The weighted-AIRS radiances are summed, and are converted to T_b. All AIRS channels within the MODIS SRF are used except

those with excessive noise determined by the AIRS channel properties file and manual inspection.

[14] Figure 3 shows scatterplots of the individually matched AIRS and MODIS cloud top pressure (P_C), T_C, and f for the granule shown in Figure 2. It is immediately apparent that, although the same collocation methodology was applied, the pixel-scale agreement between AIRS and MODIS P_C, T_C, and f is poor. To explore the reasons for the disagreement, we consider the AIRS operational quality control parameters. One such parameter, "RetQA", indicates the degree of convergence in the AIRS/AMSU retrieval algorithm and is nonzero when cloudiness is highly correlated in adjacent footprints (for example, high values of f_A in the 3 × 3 AIRS array) [*Susskind et al.*, 2006] (see Appendix B for specific details on RetQAFlag). A second parameter, "retrieval type", indicates failure in one of the retrieval steps, and is nonzero for precipitating clouds. The spectrum of possible RetQAFlag values are combined into three coarse "categories": category 1 is known as "confident with sea surface temperature over ocean", category 2 as "retrieval type = 0", and category 3 as "retrieval type $\neq$ 0." In general, the cloud amount and opacity increases from
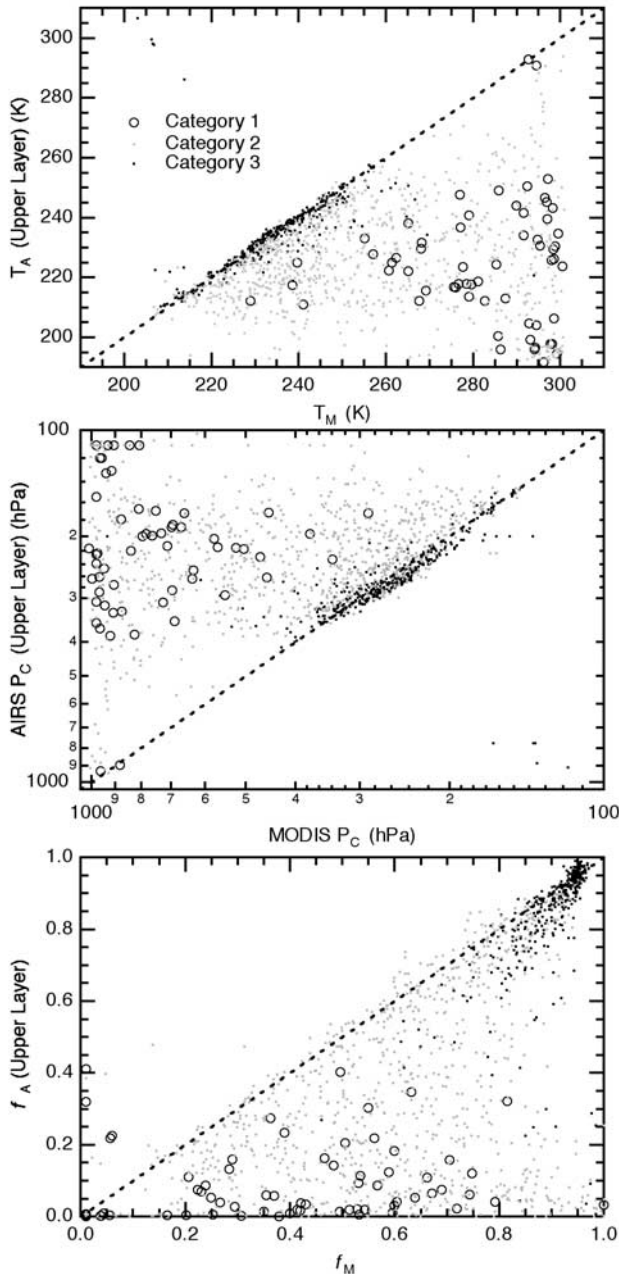
Figure 3. (a) Comparison of AIRS (upper level) and MODIS T_C. The comparison is subdivided into three categories based on the AIRS RetQAFlag. (b) Comparison of AIRS (upper level) and MODIS P_C. (c) Comparison of AIRS (upper level) and MODIS f.

category 1 to 3, but homogeneous low cloudiness can fall into category 2. Figure 3 demonstrates that high and opaque clouds, black points indicating category 3 pixels, have the best agreement in P_C, T_C, and f for AIRS and MODIS. This result is consistent with the sensitivity of CO_2 slicing methods: T_C and f for high and opaque clouds are retrieved with greater accuracy, in general, than for lower and transparent/broken clouds [*Wielicki and Coakley*, 1981],

or multilayer clouds [*Baum and Wielicki*, 1994]. On the other hand, the category 1 and 2 pixels in Figure 3 show large disagreement for most FOVs.

[15] As Figure 3 shows, a head-to-head comparison of individual cloud quantities (for example, Z_A to Z_M, T_A to T_M, and f_A to f_M) is not necessarily straightforward because of the different number of cloud layers retrieved, differences in the detected cloud fields, and algorithmic details of the retrieval. Therefore in the following section, we combine T_C, f, and T_S to construct an "effective scene brightness temperature", $T_{b,e}$, separately for AIRS ($T_{b,e}^A$) and MODIS ($T_{b,e}^M$) to help assess the radiative consistency between the retrievals from the two instruments. In this work, we emphasize $T_{b,e}$ as an additional constraint in cloud product comparisons and as a diagnostic tool for retrieval performance of particular cloud fields.

2.3. Constructing $T_{b,e}$ From Retrieved Clouds

[16] One way to compare cloud products between different instruments is to perform a radiative transfer (RT) calculation over a spectral interval for each instrument's retrieved state and compare the calculated radiances. In this type of comparison, the radiances have frequency dependence. Since the cloud retrieval problem is, in general, ill-posed, a set of cloud parameters derived from one spectral interval might not necessarily be consistent with cloud parameters derived from a different spectral interval for the same instrument [*L'Ecuyer et al.*, 2006]. This is especially true if the Planck function is highly nonlinear at T_C for one or more of the spectral intervals of interest. Therefore for comparison purposes, it is desirable to select a spectral interval removed from those used to derive the cloud properties. Additionally, it is desirable that the spectral region be mostly sensitive to cloud properties, and not to background atmospheric composition, thermal structure, and surface characteristics.

[17] For these reasons we use an idealized long-wavelength limit RT calculation where the Planck function is linear over the range of $T(z)$ from the surface to cloud top, surface and cloud effective emissivity are unity, the effective reflectivity is zero and the cloud-free air is perfectly transmissive. In such a regime, the equation for upwelling thermal IR radiance for a two-cloud system (as retrieved by AIRS) is:

$$T_{b,e}^A = f_1 T_1 + f_2 T_2 + (1 - f_1 - f_2)T_S, \qquad (1)$$

where $T_{b,e}^A$ is the AIRS $T_{b,e}$, T_i is the retrieved cloud top temperature for layer i, and f_i is the retrieved fraction of the FOV with T_i. In the single-layered cloud system (as retrieved by MODIS), the equation has the form:

$$T_{b,e}^M = f_1 T_1 + (1 - f_1)T_S. \qquad (2)$$

We emphasize that f_i is an effective cloud fraction (cloud fraction × cloud emissivity), so these relationships hold for semitransparent cloud layers.

[18] Equations (1) and (2) can be derived in the following manner. For one-dimensional (1-D) RT problems, the observed radiance I of a given footprint (or pixel) is the sum

of the radiances from i emitting areas (I_i) weighted by f_i of the emitting layer [e.g., *Liou*, 2002],

$$I = \sum f_i I_i. \qquad (3)$$

In the longwave limit, the relationship between the Planck function and the temperature of an emitting layer is approximately linear, which allows us to state

$$T_{b,e} = B_\nu^{-1}\left[\sum_i f_i B_\nu(T_i)\right], \qquad (4)$$

where $B_\nu(T_i)$ is the Planck function of an emitting layer with T_i, and B_ν^{-1} is the inverse Planck function. This can be rewritten as

$$T_{b,e} = \sum f_i T_i. \qquad (5)$$

[19] In simple terms, $T_{b,e}$ is the sum of all emitting layers, with each layer weighted by the effective fractional area. The summation in equation (5) can be expanded to one- and two-layered (or more) cloud systems with a surface contribution, represented by equations (1) and (2) for AIRS and MODIS, respectively.

[20] It should be mentioned that $T_{b,e}$ is an approximation. Note the frequency-dependence of the Planck function and the lack of nonlinearity in equations (1) and (2). Since the spectral channels used in AIRS and MODIS cloud retrievals are not in the longwave limit (cf., Figure 1), the potential effects of nonlinearity must be assessed. To summarize, the frequency dependence of the Planck function increases at shorter wavelengths in equations (1) and (2). A detailed discussion and analysis of the effects of nonlinearity is presented in section 3.2.2. Our findings indicate that the overall magnitude of the nonlinearity is small and does not significantly impact the use of equations (1) and (2) in this study.

[21] Taking the difference between AIRS and MODIS $T_{b,e}$ ($\Delta T_{b,e} \equiv T_{b,e}^A - T_{b,e}^M$) is an approximate and first-order method for comparing the radiative consistency of satellite-derived cloud products. An example of $T_{b,e}^A$ is shown in Figure 2c, while $\Delta T_{b,e}$ is shown in Figure 2d. To construct Figures 2c and 2d, we require the aggregation of the 5-km resolution T_M and f_M fields to the AMSU FOV (the spatial scale of reported T_A); f_A is likewise averaged from the 3×3 AIRS array to the AMSU FOV. After MODIS cloud products are collocated to the AMSU FOV, an average of T_M, f_M, and T_S over the 45-km scale is taken. All values are weighted equally in the average.

[22] The most obvious differences between the brightness temperature difference ΔT_b in Figure 2b and the effective scene brightness temperature $\Delta T_{b,e}$ in Figure 2d are the increased magnitude and spatial coherency in $\Delta T_{b,e}$ over ΔT_b. Since a few of the spatial patterns in Figures 2b and 2d appear to coincide, the collocation approach may explain a small amount of the variation of $\Delta T_{b,e}$. On the other hand, the mixture of negative and positive differences of ΔT_b between adjacent FOVs in Figure 2b and the more consistent biases of $\Delta T_{b,e}$ over several FOVs in Figure 2d show that systematic differences unrelated to the collocation approach

cause most $\Delta T_{b,e}$ variability. Also, note that $T_{b,e}$ is slightly larger than T_b^{960} in the warmest (and clearest) FOVs, showing the effects of a perfectly transmissive atmosphere.

3. Results

[23] In this section, AIRS and MODIS $T_{b,e}$ are compared for the granule presented in Figure 2. First, $\Delta T_{b,e}$ is related to heterogeneous cloud features within the granule. Second, a particular area of disagreement (boxed area in Figure 2) is highlighted and reasons for $\Delta T_{b,e}$ variability within it are presented. We will explore the differences and how they relate to the AIRS and MODIS retrieval types, heterogeneity of MODIS cloud within the AIRS footprint, the presence of overlapping clouds, and other possible reasons. Last, four additional granules are shown to explore the general applicability of $\Delta T_{b,e}$.

3.1. Comparing AIRS and MODIS $T_{b,e}$

[24] Figure 4 summarizes $\Delta T_{b,e}$ for the three categories of AIRS RetQAFlag (described in Appendix B and summarized in section 2.2). The poor agreement in individual AIRS and MODIS cloud products (Figure 3) is greatly reduced when they are presented as $T_{b,e}$, indicating that the retrievals from the two instruments are more consistent than might be implied from inspection of Figure 3. This suggests that the large differences shown in Figure 3 are due to algorithmic differences in the retrievals, rather than instrument inconsistencies. In this section, we consider some potential physical reasons for these differences.

[25] The smallest $\Delta T_{b,e}$ is observed for category 3 retrievals, in other words, high and opaque clouds. Note the cluster of points (7 out of 1350 retrievals per AIRS granule) in the upper left of Figure 4a. These points come from pixels in the center of tropical cyclone Ele and are caused by precipitation contaminating the AIRS/AMSU retrievals. The scatter for category 2 $\Delta T_{b,e}$ is larger than category 3. The higher T_b implies that the clouds in category 2 are lower in altitude, optically thinner, and/or partially fill the AMSU FOV. As discussed earlier in section 2, such clouds have increased errors in inferred T_C and f. The scatter in categories 1 and 2 is similar. However, a cluster of points is observed near the maximum $T_{b,e}$ with $\Delta T_{b,e} \approx 0$, suggesting generally clear-sky conditions, low-level cloud, or very thin and/or broken cloud cover. Category 1 retrievals have the highest quality temperature and humidity profiles, but less skill for T_A and f_A. On the other hand, category 3 retrievals are among the most skillful for T_A and f_A as shown by the small $\Delta T_{b,e}$, but in these cases, profiles of temperature and humidity from AIRS are retrieved with less precision [*Fetzer et al.*, 2006; *Susskind et al.*, 2006].

[26] Another distinct feature in Figure 4a is the positive bias of $\Delta T_{b,e}$ between 270 and 295 K. Because MODIS retrievals are at much higher spatial resolution than AIRS, the 1σ variability of cloud top height (Z_M) within the AMSU FOV can be used as a proxy for cloud heterogeneity (Figure 4b). A scale height of 8 km is used to convert P_M to Z_M. While the conversion is not exact, it is sufficient to demonstrate the relative variability in Z_M. Inspection of Figures 4a and 4b shows that the variability in Z_M and $\Delta T_{b,e}$ are correlated. FOVs with high and opaque clouds, stratus,
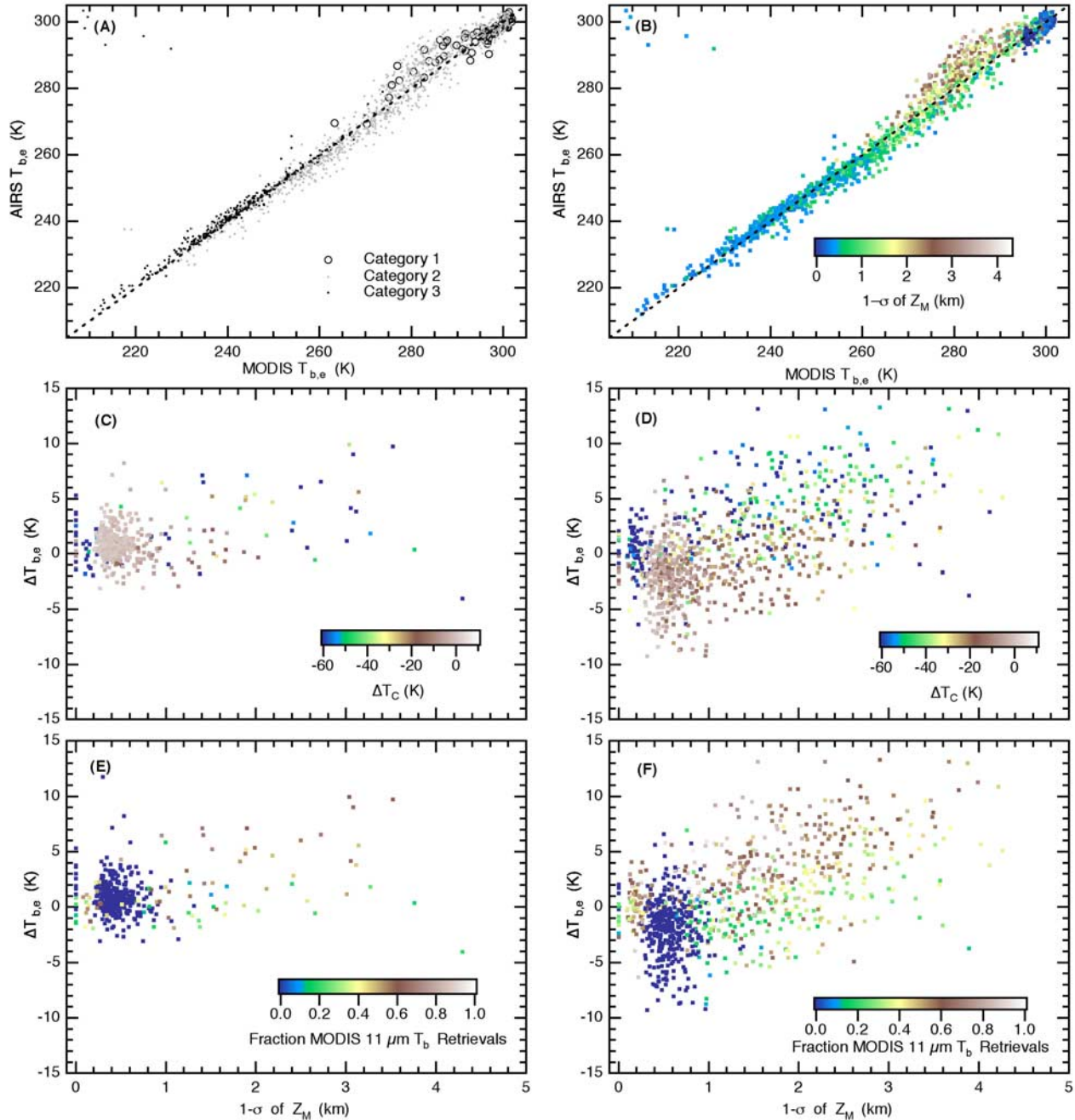
Figure 4. (a) $\Delta T_{b,e}$ on the scale of the AMSU FOV for the granule used in Figures 1, 2, and 3, which is partitioned into three general categories of AIRS retrieval type. (b) As in (a), except colors indicate 1σ variability of Z_M (km). (c) The 1σ variability of Z_M vs. $\Delta T_{b,e}$, with ΔT_C colorized; shown are categories 1 and 3. (d) As in (c) except for category 2 only. (e) The 1σ variability of Z_M vs. $\Delta T_{b,e}$, with the fraction of MODIS T_b^{11} retrievals colorized; shown are categories 1 and 3. (f) Same as (e) except restricted to category 2.

and clear sky have the least variability in Z_M because such scenes are generally homogeneous.

[27] The bias in $\Delta T_{b,e}$ is related to large differences in AIRS and MODIS T_C (ΔT_C), in addition to cloud heterogeneity, in Figures 4c and 4d. Figure 4c is a combination of categories 1 and 3, while Figure 4d is restricted to category 2 to show more clearly AIRS intercategory differences. In regions of significant cloud heterogeneity, T_A is less than T_M

by more than 60 K, while $\Delta T_{b,e}$ can range between 10 and -5 K. Additionally, significant (and negative) ΔT_C is observed in the warmest FOVs containing little to no heterogeneity in Z_M. This is suggestive of the occurrence of thin cirrus misclassified by the MODIS retrieval algorithm as low and opaque cloud. *Dessler and Yang* [2003] showed that MODIS does not detect much of the cirrus less than $\tau_{\mathrm{VIS}} = 0.2–0.3$. *Kahn et al.* [2007] show that Z_A is
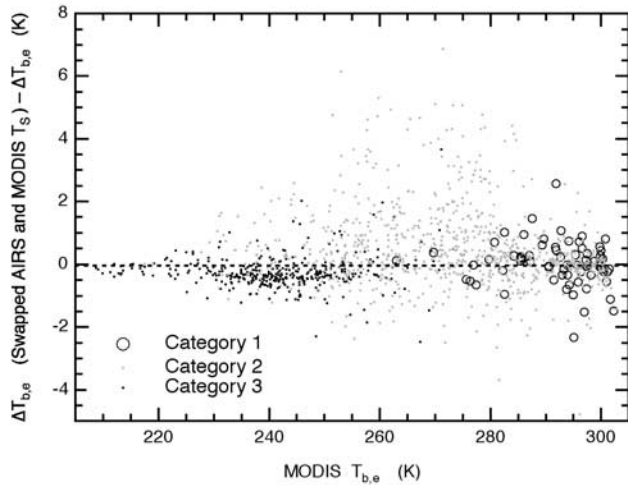
Figure 5. Difference between $\Delta T_{b,e}$ in Figure 4 and a recalculated version of $\Delta T_{b,e}$ versus $T_{b,e}^M$. To recalculate $\Delta T_{b,e}$ the AIRS and MODIS T_S fields were swapped between equations (1) and (2).

statistically significant for $f_A \geq 0.05$, approximately equal to $\tau_{VIS} \geq 0.1$. Therefore it is probable that AIRS is detecting some thin cirrus that MODIS misclassified as low and opaque cloud.

[28] Note that $\Delta T_{b,e} = 0$ does not guarantee agreement for both T_C and f; a range of solutions to T_C and f can produce the same value of $T_{b,e}$. For instance in equation (2), if T_C is reduced, then f could be reduced by an amount that keeps $T_{b,e}$ constant. A particular example of this effect is the missed detection of cirrus by MODIS that is detected by AIRS. Therefore the bias of $\Delta T_{b,e}$ in Figure 4a points to a discrepancy between AIRS and MODIS cloud retrievals that is not fully explained by compensating errors in T_C and f.

[29] Figures 4e (categories 1 and 3) and 4f (category 2) relate the MODIS retrieval method discussed in section 2 to $\Delta T_{b,e}$ by color-coding the fraction of T_b^{11} retrievals within each collocated AMSU FOV. The larger values of $\Delta T_{b,e}$ in the 270–295 K range correlate well with the increased fraction of T_b^{11} retrievals. In Figures 4e and 4f, the clusters of FOVs with 100% MODIS CO_2 slicing have little heterogeneity in Z_M ($1\sigma < 1$ km) and a small bias in $\Delta T_{b,e}$; similar behavior for FOVs near 100% T_b^{11} retrievals is noted, although a small negative bias in $\Delta T_{b,e}$ is observed for some of these FOVs. For category 1 and category 2 AIRS retrievals, heterogeneous FOVs have an increasing percentage of T_b^{11} retrievals for increasing positive values of $\Delta T_{b,e}$ which asymptotes near 60–80%.

[30] Figure 5 quantifies the potential impact of erroneous T_S on $T_{b,e}$. The AIRS and MODIS T_S fields are interchanged between equations (1) and (2) and $T_{b,e}$ is recalculated; we use the "swapped" fields of T_S as a proxy for the magnitude of uncertainty in T_S. The results are shown in Figure 5. The difference between $\Delta T_{b,e}$ presented in Figure 4 and the recalculated version of $\Delta T_{b,e}$ is plotted as a function of $T_{b,e}^M$ for the three categories of AIRS retrieval type. The change in magnitude of $\Delta T_{b,e}$ for most FOVs is within ± 1 K, several times less than the scatter of $\Delta T_{b,e}$ observed

in Figure 4. Thus, the surface contributes at most marginally toward the observed biases and scatter in $\Delta T_{b,e}$ shown in Figure 4.

[31] To further understand the correlations between the heterogeneity of cloud cover with the method of Z_M retrieval and the bias in $\Delta T_{b,e}$, section 3.2 focuses on the highlighted region shown in Figure 2.

### 3.2. Reasons for Biases in $\Delta T_{b,e}$
3.2.1. Scene Complexity

[32] Figure 6 illustrates the spatial correlation of variability in $\Delta T_{b,e}$ to Z_M within the focus region of Figure 2. In Figures 6a–6c, cloud-free regions, as classified by MODIS, are shown in white. Figure 6a shows MODIS cloud fraction f_M, revealing a complex scene centered on broken opaque clouds (f_M near 1) that are surrounded by optically thinner clouds ($f_M < 0.5$). A comparison of T_M (Figure 6b) to f_M demonstrates that the broken opaque cloud tops are close to the surface (near 300 K), whereas thinner clouds are much higher (near 230 K). In Figure 6c the method of MODIS cloud retrieval is shown. Patterns of T_b^{11} and CO_2 slicing retrievals correlate with cloud features throughout the region. The $T_{b,e}^M$ for the scene shown in Figure 2c is expanded for the focus scene in Figure 6d, and $\Delta T_{b,e}$ is presented in Figure 6e. Along the borders of the high and low clouds, $\Delta T_{b,e}$ is positive and large. The magnitude of ΔT_C is largest in these border regions as shown in Figure 6f. However, differences in ΔT_C are not always positively correlated with $\Delta T_{b,e}$ since Δf contributes to the disagreement, as seen in equations (1) and (2). Figure 6 demonstrates that positive biases in $\Delta T_{b,e}$ are spatially correlated to heterogeneous FOVs with mixtures of T_b^{11} and CO_2 slicing retrievals for MODIS.

[33] The 1-km MODIS radiances are considered in a false color image, shown in Figure 7a, to understand whether regions of large and positive differences in $\Delta T_{b,e}$ coincide with overlapping clouds. To highlight differences in cloud phase, the MODIS 0.65-μm reflectance (band 01) is mapped to red, 2.1-μm reflectance (band 07) is mapped to green, and T_b^{11} (band 31) is mapped to blue. Ice clouds tend to be purple, while water clouds tend toward yellow, but can tend toward pink if they are opaque and relatively cold. Figure 7a shows that low-level clouds are mostly small-scale cumulus. Thus, areas of opaque ice cloud and thin cirrus co-exist with patches of overlapping thin cirrus and cumulus clouds, consistent with the region's cloud climatology.

[34] Figure 7b marks (in color) pixels likely containing thin cirrus overlapping low-level water clouds using the algorithm described by *Nasiri and Baum* [2004]. Three MODIS bands at 2.1, 8.5, and 11 μm and the cloud mask [*Ackerman et al.*, 1998] are used to identify overlapping clouds. Pixels are classified as overlapping on a pixel-by-pixel basis, but statistics regarding adjacent pixels are used in the classification process. The color scale indicates the number of times a pixel is classified as overlapping based on nearby pixel statistics. A careful visual examination of MODIS radiances indicates that the algorithm by *Nasiri and Baum* [2004] is detecting a majority of the overlapping thin cirrus and low-level water clouds, although false positives may occur at 19°W and 189°E. Figure 7b shows that much of the large and positive $\Delta T_{b,e}$ seen in Figure 6e corre-
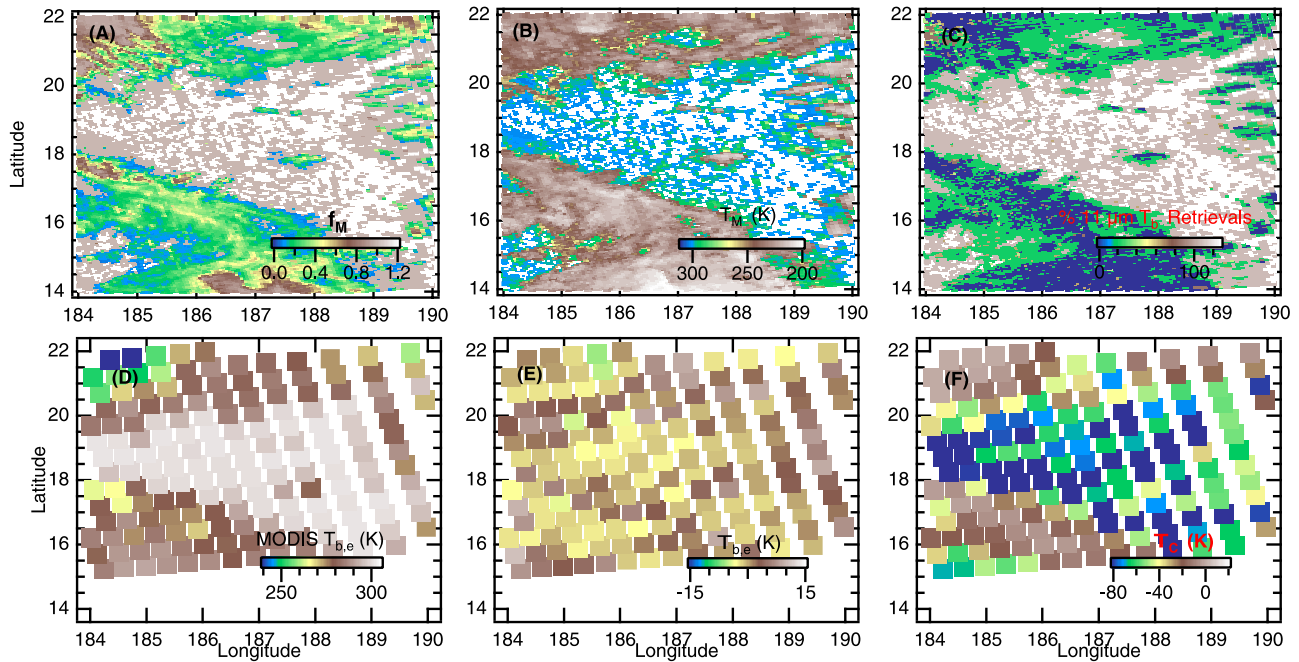
Figure 6. (a) f_M. (b) T_M (K). (c) Method of T_M retrieval; $100 = T_b^{11}$, $0 \leq CO_2$ slicing method >100 are for the five different slicing pairs, and white = clear sky. (d) $T_{b,e}^M$ for focus region in Figure 2. (e) $\Delta T_{b,e}$ (K). (f) ΔT_C (K).

sponds to areas of overlapping clouds, where mixtures of T_b^{11} and CO_2 slicing retrievals occur.

[35] The scene variability is related to the MODIS cloud mask in Figure 7c. A scatterplot of MODIS 2.1-μm reflectance versus T_b^{11} is shown for the four cloud mask confidence intervals. The filled "triangle" of points demonstrates that distinct cloud layers cannot be separated from one another, and a large amount of variability in T_b^{11} of the clear-sky pixels exists. The 10-K variation in clear sky T_b^{11} shown in Figure 7c is larger than the sea surface temperature variability and suggests undetected thin cirrus.

[36] The effects of cloud variability and overlap on T_M are considered in Figure 7d. The frequency distribution of T_M is shown in the upper panel for 5-K bins. A bimodal distribution corresponding to low-level water clouds and high ice clouds is seen. In the lower panel, the fraction of T_M in each bin with overlapping clouds is shown. If at least 5 of 25 pixels within a 5×5 km region have a high likelihood of overlapping cloud, the T_M pixel is described as containing overlapping clouds. The lower panel of Figure 7d shows that a majority of MODIS pixels with $260 < T_M < 280$ K have overlapping clouds (with a significant minority to 290 K), and they generally correspond to the warm bias in $\Delta T_{b,e}$ between 270–295 K in Figure 4. This suggests that different treatments of overlapping cloud in the AIRS and MODIS retrieval algorithms may explain some of the discrepancy in $T_{b,e}$.

3.2.2. Nonlinearity of $T_{b,e}$

[37] As discussed in section 2.3, $T_{b,e}$ is calculated from partial FOV contributions of T_C and T_S weighted by f and $(1 - f)$, respectively, using the longwave approximation, which does not account for potential nonlinear effects. Since cloudy radiances have some frequency dependence,

the set of cloud parameters derived from AIRS and MODIS may not be consistent based solely on the choice of channels used in the retrieval [*L'Ecuyer et al.*, 2006]. If poor fits are obtained between simulated and observed radiances, this effect may be enhanced.

[38] Figure 8 demonstrates the effects of nonlinearity for particular spectral intervals (4.2, 9, and 14 μm) used in AIRS and MODIS cloud retrievals. Using these wavelengths $T_{b,e}$ is recalculated using equation (4) where the Planck function is calculated for each surface and cloud layer for AIRS and MODIS separately. Then, the inverse Planck function is calculated for the linear sum of the area-weighted Planck radiances. Figures 8a–8c show that the primary feature of disagreement in Figure 4, the warm bias from 270 to 295 K (discussed in sections 3.1 and 3.2.1), exists at all calculated wavelengths. The effects of nonlinearity are stronger at 4.2 μm than at 9 and 14 μm as evidenced by the larger spread in the distribution; however, Figure 8 demonstrates that the discrepancy that is attributed to mixed and overlapping cloud scenes is not due to nonlinear effects.

[39] The nonlinearity in MODIS cloud retrievals most closely resembles that around 14 μm and in the window channels (Figures 8b and 8c) since they form the basis of the CO_2 slicing and window cloud retrievals. In the case of AIRS, the nonlinearity is a blend of the 14- and 4-μm channels (Figures 8a and 8b); thus, the total effect is not as dramatic as the 4.2-μm region alone. Additionally, there is a tendency for the coldest clouds to increase in $T_{b,e}$ with decreasing wavelength. This occurs because of the decrease in radiance with shorter wavelength in cold scenes; they contribute a smaller portion to the area-averaged radiance. Last, note that the scatter in $\Delta T_{b,e}$ increases at
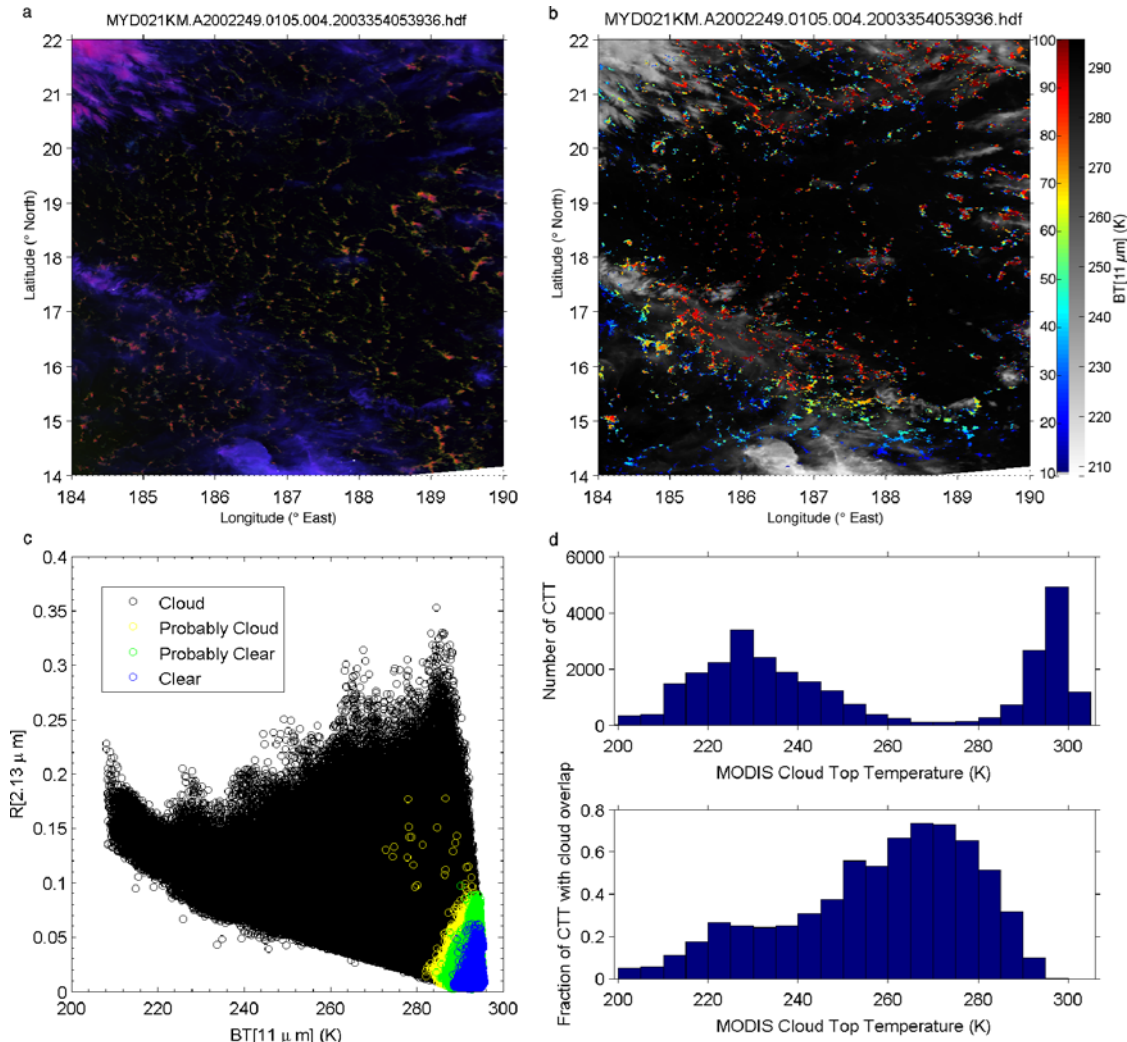
Figure 7. (a) False color image of region shown in Figure 5. MODIS 0.65 μm reflectance (band 01) is mapped to red, 2.1 μm reflectance (band 07) as green, and T_b^{11} (band 31) to blue. (b) Pixels likely containing thin cirrus overlapping lower level water clouds according to *Nasiri and Baum* [2004] (in color), overlaying T_b^{11}. (c) Scatterplot of MODIS 2.1 μm reflectance versus T_b^{11} for four cloud mask confidence intervals. (d) Distribution of retrieved T_M in 5-K bins (upper panel), and the fraction of T_M retrievals with overlapping clouds (lower panel).

the shorter wavelengths. However, the bias in the warmer scenes is still identifiable through the increasing scatter, even at 4.2 μm.

3.2.3. Additional Factors

[40] There are other possible contributors to the bias in $\Delta T_{b,e}$. These include the method of averaging MODIS cloud products to the AMSU FOV and radiative effects not accounted for in 1-D RT algorithms. In a comparison study of AIRS and Atmospheric Radiation Measurement (ARM) program-derived Z_C by *Kahn et al.* [2007], the mean bias and variability in the agreement of AIRS and ARM Z_C were shown to be a function of the averaging methodology of ARM Z_C. That study included the use of average Z_C, the maximum Z_C, or histograms to identify the peak frequency in Z_C over a variable length time window. As a result, an average of MODIS cloud products (as performed in this study) to the AMSU FOV is expected to be another poten-

tial source of variability in $\Delta T_{b,e}$, and is a topic of future research.

[41] Cloud property retrievals based on plane-parallel infrared RT theory are poorly suited for pixels containing partial cloud coverage [*Coakley et al.*, 2005] and inhomogeneous cloud structure [*Liou and Ou*, 1979; *Harshvardhan and Weinman*, 1982]. Inhomogeneous clouds are not necessarily blackbodies in the IR, even as τ_{IR} approaches large values. By using window techniques that assume black cloud (for example, the MODIS T_b^{11} retrieval), erroneously high T_C (low Z_C) is retrieved. Evidence for this effect in stratocumulus clouds is presented by *Coakley et al.* [2005] and *Cornet et al.* [2005]. With regard to cirrus, horizontal inhomogeneities of τ_{IR} within a satellite pixel can cause biases in outgoing longwave radiation [*Fu et al.*, 2000]. Although it is beyond the scope of this work to quantita-
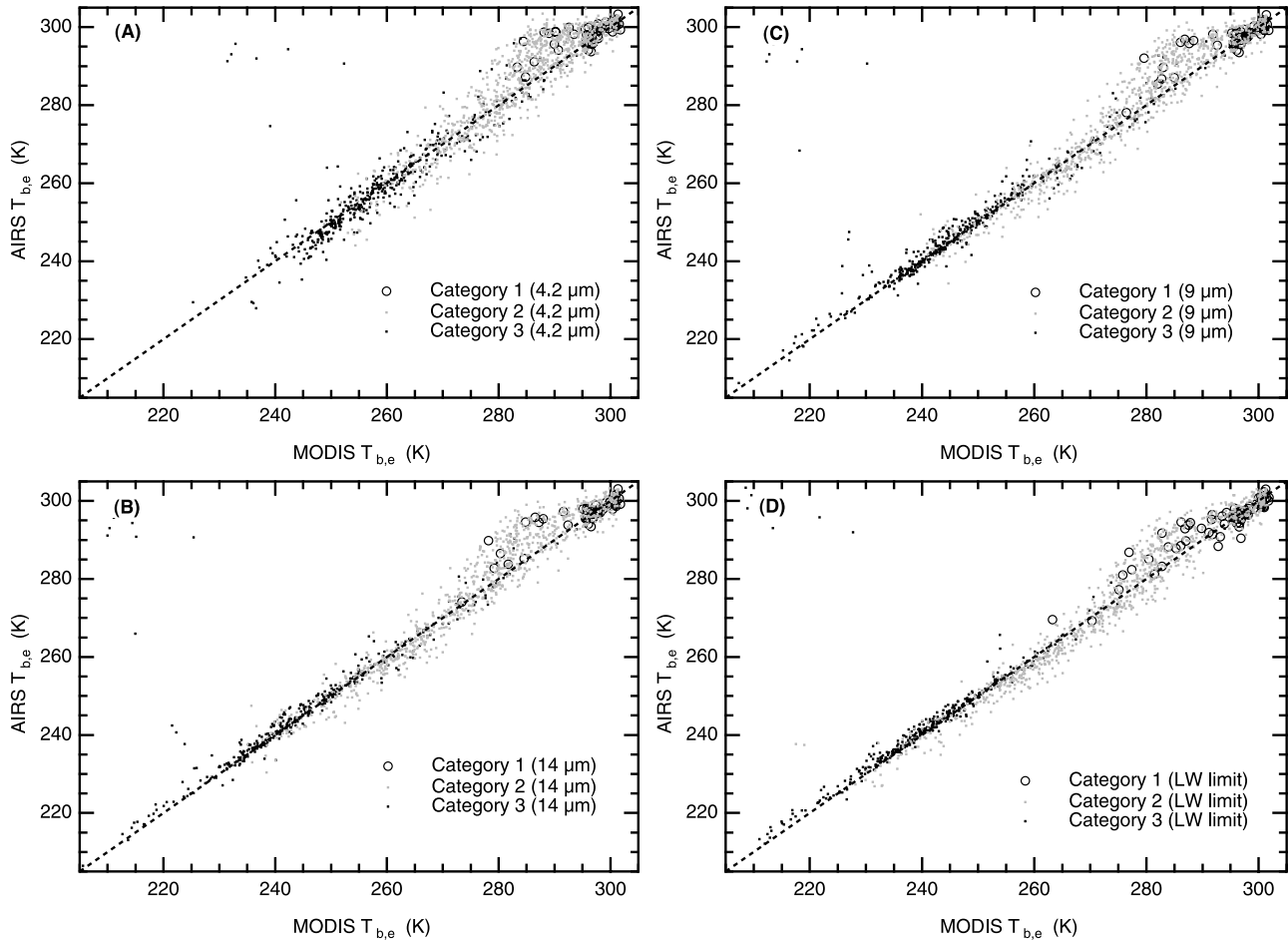
Figure 8. $\Delta T_{b,e}$ for three categories of AIRS retrieval type, as in Figure 4a, except for (a) 4.2 μm, (b) 9 μm, and (c) 14 μm. (d) is a repeat of Figure 4a (for the longwave limit), shown again for comparison purposes.

tively relate pixel-scale partial cloud coverage and inhomogeneity to $\Delta T_{b,e}$ variability, observational results and modeling studies suggest they could cause some variability in $\Delta T_{b,e}$.

3.3. How Consistent is $\Delta T_{b,e}$ Elsewhere?

[42] To explore the global characteristics of AIRS and MODIS $T_{b,e}$, approximately 20 granules have been inspected from 6 September 2002. In Figure 9, four additional AIRS granules demonstrate $\Delta T_{b,e}$ for meteorologically diverse locations: the midlatitude southern and northern hemispheres (SH and NH, respectively), the tropical eastern Pacific Ocean along the coast of South America, and the tropical south Pacific. In summary, the behavior of $\Delta T_{b,e}$ is consistent between Figures 2 and 9, although there are important scene-dependent differences.

[43] Figures 9a–9c shows the AIRS T_b^{960}, $\Delta T_{b,e}$, and a scatterplot of AIRS and MODIS $T_{b,e}$ as a percentage of T_b^{11} retrievals. This granule is located in the midlatitude SH and is dominated by uniform cloudiness with 240 K $< T_b^{960} <$ 290 K. The positive bias in $\Delta T_{b,e}$, demonstrated in Figure 4, is not observed in Figure 9c. A region of enhanced scatter exists in $\Delta T_{b,e}$ (negative and positive) from 270 to 280 K, and appears to be correlated to the percentage of T_b^{11}

retrievals. The absence of a significant bias in $\Delta T_{b,e}$ is observed elsewhere in high-latitude regions. Positive biases in $\Delta T_{b,e}$ tend to be largest in tropical scenes, and they decrease in magnitude with increasing latitude toward the SH and NH poles. Thus, the discrepancy of AIRS and MODIS cloud fields illustrated in Figures 2 and 4 could be greatest in the tropical latitudes. Conversely, in the high latitudes, smaller $\Delta T_{b,e}$ suggests that head-to-head comparisons of individual cloud quantities (T_C and f) may be more straightforward.

[44] In Figures 9d–9f, a scene in the SH central tropical Pacific is presented. It is primarily composed of broken and thin cloudiness, including cirrus and cumulus, with a notable absence of low T_b^{960} suggesting deep convection. The largest biases in $\Delta T_{b,e}$ occur along cirrus edges, as seen in Figure 2. The warmer FOVs of low-level cumulus and/or clear sky containing 100% T_b^{11} retrievals are clustered near $\Delta T_{b,e} = 0$, with scatter of a few degrees. This behavior is consistent with FOVs in Figure 4b that contain 100% T_b^{11} retrievals. A granule in the midlatitude NH including a tail end of a frontal zone is presented in Figures 9g–9i. It is similar to the granule in the SH midlatitude, but the lower latitude FOVs are warmer, and a suggestion of a positive bias in $\Delta T_{b,e}$ near 265–275 K exists. The FOVs with
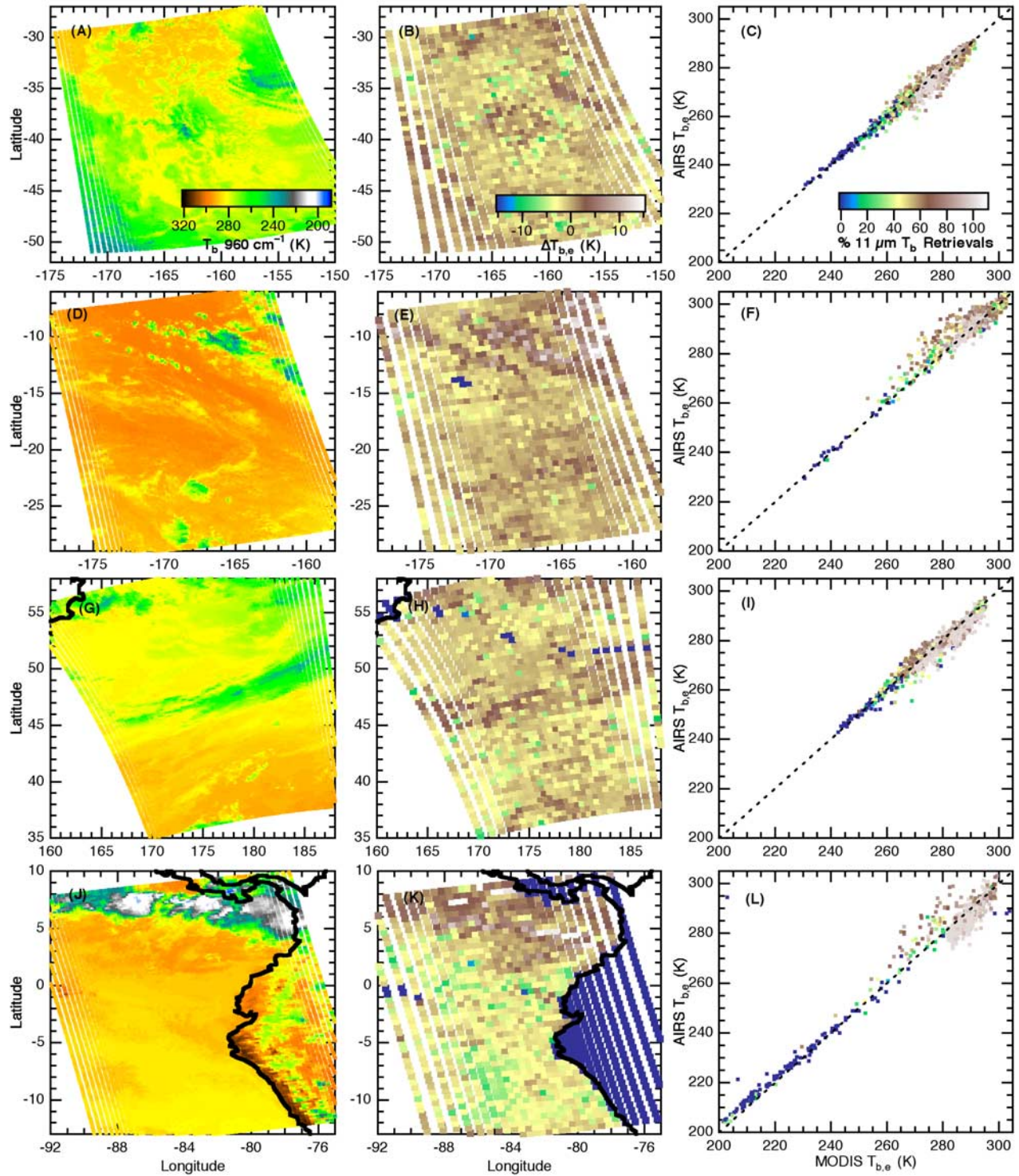
Figure 9. (a) AIRS T_b^{960} (K) for granule 8 (0042 UTC) on 6 September 2002. (b) $\Delta T_{b,e}$ (K) for the granule in (a). (c) Scatter of $\Delta T_{b,e}$ as a function of the percentage of T_b^{11} retrievals for the granule in (a). (d)−(f) Same as (a)−(c) except for granule 9 (0048 UTC). (g)−(i) Same as (a)−(c) except for granule 12 (0106 UTC). (j)−(l) Same as (a)−(c) except for granule 191 (1900 UTC). The color bars in (a)−(c) apply to (d)−(l).

100% T_b^{11} retrievals cluster around $\Delta T_{b,e} = 0$ from 265 to 295 K. The 100% CO_2 slicing FOVs have a small negative $\Delta T_{b,e}$ bias no larger than 1−2 K. Thus, it appears that discrepancies between AIRS and MODIS cloud fields are a function of cloud type, which is exaggerated at the lowest latitudes, a region exhibiting the greatest range of potential cloud types occurring together (for example, cirrus and trade cumulus).

[45] The last sample granule is located along the western coast of South America (Figures 9j–9l). The eastern Pacific is dominated by a stratocumulus layer south of $2-3°N$, with the Intertropical Convergence Zone (ITCZ) located from $5°$ to $10°N$. The positive bias in $\Delta T_{b,e}$ is significant along the southern (and northern) edge of the ITCZ, where the convection transitions into low-level cumulus. As in Figure 2, positive biases in $\Delta T_{b,e}$ occur in FOVs with a mixture of T_b^{11} and CO_2 slicing retrievals. In the stratocumulus to the south, a negative bias of $2-5$ K exists that is slightly larger (smaller) in some FOVs with slightly lower (higher) T_b^{960}. In the neighboring granule to the south (not shown), the negative bias is reduced to $0-2$ K. In the retrieval of T_M using T_b^{11}, $T(z)$ profiles generated by numerical weather prediction models are used to assign the T_b^{11} to Z_M [Menzel et al., 2002]. Thus, any biases in model-calculated $T(z)$ are reflected in T_M [Kahn et al., 2007]. In regions such as these that contain strong atmospheric inversions, significant errors in cloud top height can be made due to the structure of the atmospheric $T(z)$ profiles.

3.4. Practical Considerations of $T_{b,e}$

[46] Many end-users of AIRS and MODIS are not necessarily concerned with all details of the cloud retrieval algorithms, but they do require a measure of their accuracy and precision. Calculated $T_{b,e}$ fields provide an approximate yet rapid assessment of the consistency of some cloud properties obtained from independent measurements and/ or algorithm methods. This approach has been demonstrated herein with AIRS and MODIS onboard EOS Aqua and is generically applicable to other instrument platforms that retrieve T_C and f. As discussed in section 1, the agreement in $T_{b,e}$ is a necessary, but not a sufficient, condition for individual agreement in AIRS and MODIS T_C and f. For scenes where AIRS and MODIS $T_{b,e}$ disagree, the end-user is cautioned that either (or both) cloud fields may be problematic. For scenes in which AIRS and MODIS $T_{b,e}$ agree, the individual fields (T_S, T_C, and f) may be different such that they compensate to produce the same $T_{b,e}$, which requires further comparison of T_S, T_C, and f individually.

[47] In sections 3.1, 3.2, and 3.3, we showed (1) the existence of a bias in AIRS-MODIS $\Delta T_{b,e}$, (2) a correlation of the $\Delta T_{b,e}$ bias with heterogeneous scenes and multilayered/ overlapping cloud, (3) AIRS and MODIS cloud retrieval algorithm differences dominate collocated radiance uncertainties, and (4) AIRS and MODIS $T_{b,e}$ agree most closely in uniform scenes. The bias in $\Delta T_{b,e}$ and its correlative relationship to complicated cloud configurations are indicative of an inconsistency in the algorithmic treatment of AIRS and MODIS cloud fields.

[48] The availability of cloud radar and lidar measurements from the surface at the Atmospheric Radiation Measurement (ARM) program sites [Ackerman and Stokes, 2003], and from space via CloudSat and CALIPSO [Stephens et al., 2002; Winker et al., 2003], will help to constrain the ambiguity of compensating effects in $T_{b,e}$. Although the surface- and space-based active measurements of cloud boundaries coincide with a small percentage of the total number of AIRS and MODIS swath observations, this subset will help to determine the capabilities and limitations of cloud fields derived from AIRS and MODIS and other passive observational platforms.

[49] The results presented herein suggest an organized collaborative effort between the assorted satellite instrument and algorithm teams (for example, AIRS and MODIS) is necessary to reconcile the differences observed in the cloud retrievals. Previous intercomparisons of algorithms applied to identical cloudy radiance data sets [Rossow et al., 1985; Wielicki and Parker, 1992] and comparisons of cloud climatologies derived from different observing platforms [e.g., Rossow et al., 1993; Thomas et al., 2004] suggest that the radiative transfer models, the retrieval algorithms and their assumptions, and ancillary data used to generate cloud fields must be carefully evaluated against one another.

4. Summary and Conclusions

[50] The consistency of cloud top temperatures (T_C) and effective cloud fractions (f) retrieved by MODIS and the AIRS/AMSU observation suite on the EOS Aqua platform is investigated. Collocated AIRS and MODIS T_C and f are compared using an "effective scene brightness temperature" ($T_{b,e}$), which is calculated for AIRS and MODIS individually from field of view (FOV) contributions of T_C and surface temperature (T_S), weighted by f. The radiance for a given FOV is the linear sum of radiances from each fractional area, represented by cloud layers and the surface. Using the longwave approximation, we replace the Planck function for each fractional area by T_C and T_S. $T_{b,e}$ is calculated by weighting T_C and T_S with the f of each cloud layer and $(1 - f)$ for the clear-sky portion of the FOV. AIRS reports up to two cloud layers whereas MODIS reports up to one; however, MODIS reports T_C, T_S, and f at a smaller spatial scale than AIRS. The use of $\Delta T_{b,e}$ allows radiative consistency comparisons to be made that help overcome some of the difficulties in pixel-scale multi-instrument comparisons of T_C and f.

[51] The poor agreement in individually matched T_C and f is greatly improved when presented as $T_{b,e}$. The smallest $\Delta T_{b,e}$ is observed for high and opaque clouds. For low altitude, transparent, and broken clouds, the $\Delta T_{b,e}$ variability increases. This is consistent with the known sensitivity of IR radiances to T_C and f [Wielicki and Coakley, 1981]. The spatial patterns of $\Delta T_{b,e}$ are systematic and are not well correlated to AIRS-MODIS radiance differences, which are more variable but smaller in magnitude than $\Delta T_{b,e}$. These results suggest that inconsistencies in AIRS and MODIS cloud fields are dominated by retrieval algorithm differences, as opposed to collocated radiance differences.

[52] A distinct feature in $\Delta T_{b,e}$ is a positive bias (AIRS > MODIS $T_{b,e}$) between 270 and 295 K. It is correlated to the degree of cloud heterogeneity within the AMSU FOV using the variability of MODIS cloud top height (Z_M) as a proxy. The most homogeneous scenes occur for high and opaque clouds, stratus, or clear scenes. In regions of heterogeneous clouds, negative AIRS-MODIS T_C (ΔT_C) is found to be in excess of 60 K. Additionally, significantly negative ΔT_C is observed in the warmest FOVs containing little to no heterogeneity in Z_M, indicating thin cirrus misplaced by MODIS as low and opaque cloud. We show that AIRS is detecting some of the thin cirrus that is misplaced by MODIS.

[53] We show the positive bias in $\Delta T_{b,e}$ is related to the MODIS retrieval method (CO_2 slicing or a window method)

[*Menzel et al.*, 2002] by considering the fraction of the 11-μm window retrievals (T_b^{11}) within each collocated AMSU FOV. The bias for 270–295 K correlates to the fraction of T_b^{11} retrievals. FOVs with mixed MODIS cloud retrieval methods are shown to correspond to overlapping cirrus and low-level water clouds. Using the algorithm by *Nasiri and Baum* [2004], a majority of T_M retrievals for 260–280 K, and a large minority up to 290 K, have overlapping clouds coinciding well to the warm bias in $\Delta T_{b,e}$.

[54] Additional granules are presented to show the consistency of $\Delta T_{b,e}$ for a variety of observational scenes, including the NH and SH storm tracks, and equatorial regions in the central and eastern Pacific Ocean. The warm bias in $\Delta T_{b,e}$ is largest in warm tropical scenes along the edges of high clouds, and decreases in magnitude toward both poles. This suggests that the discrepancy of AIRS and MODIS may be greatest in the tropical latitudes within scenes of heterogeneous cloudiness.

[55] $T_{b,e}$ will be useful as a diagnostic for satellite retrievals of T_C and f. We have shown its usefulness in finding inconsistencies between two retrieval methods. $T_{b,e}$ will also be useful to guide further comparisons of T_C and f. That other retrievals like cloud particle size, optical depth, cloud phase, and water path may require information about T_C and f stresses the importance of their evaluation and validation.

Appendix A

[56] Trigonometric relations required to collocate MODIS pixels within an AIRS FOV are presented; a schematic of the geometry is shown in Figure A1. This method is approximate since the AIRS FOV is assumed to be circular at nadir with an increasingly distorted ellipse at increasing off-nadir scan angle. In reality, the AIRS FOV is not circular, nor is the spatial response function uniform. These shortcomings are expected to have a maximum impact at off-nadir scan angles in heterogeneous cloud scenes, the effects of which are seen in Figure 2b. Future comparisons will include a more realistic FOV with a formal representation of the spatial response function.

[57] Beginning with the law of Cosines we define

$$s^2 - (2r_s \cos \alpha)s + (r_s^2 - r_e^2) = 0. \tag{A1}$$

Equation (A1) is a quadratic, and we obtain:

$$s = r_s \cos \alpha \pm \sqrt{r_e^2 + r_s^2 \sin^2 \alpha}. \tag{A2}$$

The appropriate solution requires the choice of the negative sign since the positive sign implies a nonphysical solution that passes through the Earth's surface. The slant range allows one to calculate the "spreading" of the satellite's FOV in the along-track (y) direction. Given the size of the AIRS FOV in degrees, the AIRS nadir FOV in kilometer is found by multiplying the FOV by the altitude of the satellite. For AIRS, the nadir FOV is 1.1° × 705 km = 13.535 km. For off-nadir FOVs, size in the y direction is 13.535·s/a, where s is the slant path calculated using equation (A4), and a is the nominal altitude of the Aqua satellite (705 km).
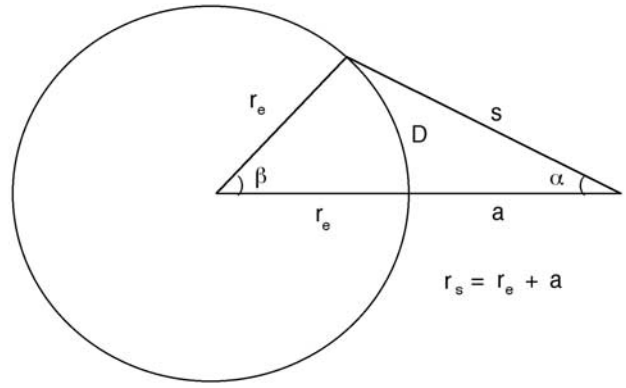
Figure A1. Geometry of a given AIRS FOV used in the collocation approach. Quantities are as follows: a is the altitude of EOS Aqua, r_e is the radius of Earth, r_s is the radial distance to Aqua, s is the slant path from Aqua to Earth's surface, α is the scan angle of AIRS, β is the earth central angle, and D is the arc distance from the subsatellite point of Aqua to the viewed point on the surface.

[58] Calculating the size of the FOV in the cross-track (x) direction requires the arc distance D. Returning to Figure A1, note that D corresponds to the size of the FOV in the x direction for the nadir view if α is taken to be one half the nadir FOV. In general, D can be found using the equation

$$D = \beta \cdot r_e, \tag{A3}$$

where β is the earth central angle and r_e is 6371 km, the mean radius of the Earth. The angle β can be found using the law of Sines,

$$\frac{r_e}{\sin \alpha} = \frac{s}{\sin \beta} \Rightarrow \beta = \arcsin\left(\frac{s \sin \alpha}{r_e}\right). \tag{A4}$$

In practice, the size of the FOV in the x direction is calculated by (1) determining s to either end of the FOV and then (2) subtracting D from the left and right sides of the FOV.

[59] Collocating the MODIS pixels within the AMSU FOV is straightforward with AIRS/AMSU and MODIS geolocation. The MODIS pixels located in between AIRS FOVs (but located within an AMSU FOV) are not included in the collocation process. This approach is justified because AIRS radiances are used to derive T_A and f_A.

Appendix B

[60] The AIRS L2 version 4 geophysical products have different levels of "quality" depending on the characteristics of the observed scene and, to a large extent, the amount and heterogeneity of cloud cover and the occurrence of precipitation [*Susskind et al.*, 2006]. A series of internal consistency checks, presented as "quality flags" in the version 4 algorithm, are performed during the cloud-clearing and retrieval process to assess the degree of convergence in the retrieval solution; they are discussed in *Olsen et al.* [2005] and *Susskind et al.* [2006]. We use RetQAFlag, a 16 bit-based integer indicating whether particular quality

flags are zero or nonzero (0: "best quality", 1: "good quality", and 2: "do not use"), and whether the steps in the cloud-clearing and retrieval process are passed, rejected, or not attempted.

[61] The value of RetQAFlag is grouped into three general categories: (1) RetQAFlag = 0, where all bits in the first and second bytes = 0, (2) RetQAFlag ≠ 0, where one or more bits in the first byte ≠ 0 (byte 1 = bits 8−15), and (3) one or more bits in the second byte ≠ 0 (byte 2 = bits 0−7). In the AIRS algorithm, category 1 is known as "confident with SST over ocean", category 2 as "retrieval type = 0", and category 3 as "retrieval type ≠ 0". The category 1 retrievals are relatively clear ocean scenes where the normally challenging T_S retrieval is deemed reliable. The category 2 retrievals are for scenes where each step in the AIRS retrieval process is successful. However, some bits of the first byte of RetQAflag may indicate that a lower altitude portion of $T(z)$ is less reliable and, hence, invalid. The yield of this category increased considerably in version 4 since portions of $T(z)$ are allowed to be invalid. The category 3 retrievals include cases where the IR retrieval fails and defaults to a microwave-only retrieval, or when the microwave retrieval fails in the presence of precipitation. Category 1 is considered an "ideal" retrieval for highly accurate $T(z)$, $q(z)$, T_S, and other quantities. However, this is not necessarily true of the cloud products [*Kahn et al.*, 2007].

References

Ackerman, T. P., and G. M. Stokes (2003), The Atmospheric Radiation Measurement program, *Phys. Today*, 56, 38–44.

Ackerman, S. A., K. I. Strabala, W. P. Menzel, R. A. Frey, C. C. Moeller, and L. E. Gumley (1998), Discriminating clear sky from clouds with MODIS, *J. Geophys. Res.*, 103, 32,141–32,157.

Aumann, H. H., et al. (2003), AIRS/AMSU/HSB on the aqua mission: Design, science objectives, data products, and processing systems, *IEEE Trans. Geosci. Remote Sens.*, 41, 253–264.

Baum, B. A., and B. A. Wielicki (1994), Cirrus cloud retrieval using infrared sounding data—Multilevel cloud errors, *J. Appl. Meteorol.*, 33, 107–117.

Coakley, J. A., M. A. Friedman, and W. R. Tahnk (2005), Retrieval of cloud properties from partly cloudy imager pixels, *J. Atmos. Oceanic Technol.*, 22, 3–17.

Cooper, S. J., T. S. L'Ecuyer, P. Gabriel, A. J. Baran, and G. L. Stephens (2006), Objective assessment of the information content of visible and infrared radiance measurements for cloud microphysical property retrievals over the global ocean: Part II. Ice clouds, *J. Appl. Meteorol. Climatol.*, 45, 42–62.

Cornet, C., J.-C. Buriez, J. Riédi, H. Isaka, and B. Guillemet (2005), Case study of inhomogeneous cloud parameter retrieval from MODIS data, *Geophys. Res. Lett.*, 32, L13807, doi:10.1029/2005GL022791.

Cracknell, A. P. (1998), Synergy in remote sensing—What's in a pixel?, *Int. J. Remote Sens.*, 19, 2025–2047.

DeSouza-Machado, S., L. L. Strow, S. E. Hannon, and J. Gou (2004), Measurements of cirrus cloud parameters using AIRS, in Remote Sensing of the Clouds and Atmosphere VIII, SPIE, Bellingham, WA.

DeSouza-Machado, S. G., L. L. Strow, S. E. Hannon, and H. E. Motteler (2006), Infrared dust spectral signatures from AIRS, *Geophys. Res. Lett.*, 33, L03801, doi:10.1029/2005GL024364.

Dessler, A. E., and P. Yang (2003), The distribution of tropical thin cirrus clouds inferred from Terra MODIS data, *J. Clim.*, 16, 1241–1247.

Fetzer, E. J., B. H. Lambrigtsen, A. Eldering, H. H. Aumann, and M. T. Chahine (2006), Biases in total precipitable water vapor climatologies from Atmospheric Infrared Sounder and Advanced Microwave Scanning Radiometer, *J. Geophys. Res.*, 111, D09S16, doi:10.1029/2005JD006598.

Fu, Q., B. Carlin, and G. Mace (2000), Cirrus horizontal inhomogeneity and OLR bias, *Geophys. Res. Lett.*, 27, 3341–3344.

Gregorich, D. T., and H. H. Aumann (2003), Verification of AIRS boresight accuracy using coastline detection, *IEEE Trans. Geosci. Remote Sens.*, 41, 298–302.

Harshvardhan, and J. A. Weinman (1982), Infrared radiative transfer through a regular array of cuboidal clouds, *J. Atmos. Sci.*, 39, 431–439.

Hong, G., P. Yang, H.-L. Huang, S. A. Ackerman, and I. N. Sokolik (2006), Simulation of high-spectral-resolution infrared signature of overlapping cirrus clouds and mineral dust, *Geophys. Res. Lett.*, 33, L04805, doi: 10.1029/2005GL024381.

Houghton, J. T., et al. (2001), *Climate Change 2001: The Scientific Basis*, 881 pp., Cambridge Univ. Press, New York.

Kahn, B. H., A. Eldering, S. A. Clough, E. J. Fetzer, E. Fishbein, M. R. Gunson, S.-Y. Lee, P. F. Lester, and V. J. Realmuto (2003), Near micronsized cirrus cloud particles in high-resolution infrared spectra: An orographic case study, *Geophys. Res. Lett.*, 30(8), 1441, doi: 10.1029/2003GL016909.

Kahn, B. H., K. N. Liou, S.-Y. Lee, E. F. Fishbein, S. DeSouza-Machado, A. Eldering, E. J. Fetzer, S. E. Hannon, and L. L. Strow (2005), Nighttime cirrus detection using Atmospheric Infrared Sounder window channels and total column water vapor, *J. Geophys. Res.*, 110, D07203, doi:10.1029/2004JD005430.

Kahn, B. H., A. Eldering, A. J. Braverman, E. J. Fetzer, J. H. Jiang, E. Fishbein, and D. L. Wu (2007), Towards the characterization of upper tropospheric clouds using AIRS and MLS observations, *J. Geophys. Res.*, 112, D05202, doi:10.1029/2006JD007336.

King, M. D., Y. J. Kaufman, W. P. Menzel, and D. Tanré (1992), Remote-sensing of cloud, aerosol, and water-vapor properties from the Moderate Resolution Imaging Spectroradiometer (MODIS), *IEEE Trans. Geosci. Remote Sens.*, 30, 2–27.

L'Ecuyer, T. S., P. Gabriel, K. Leesman, S. J. Cooper, and G. L. Stephens (2006), Objective assessment of the information content of visible and infrared radiance measurements for cloud microphysical property retrievals over the global oceans: Part I. Liquid clouds, *J. Appl. Meteorol. Climatol.*, 45, 20–41.

Lambrigtsen, B. H., and S.-Y. Lee (2003), Coalignment and synchronization of the AIRS instrument suite, *IEEE Trans. Geosci. Remote Sens.*, 41, 343–351.

Li, J., W. P. Menzel, F. Sun, T. J. Schmit, and J. Gurka (2004a), AIRS subpixel cloud characterization using MODIS cloud products, *J. Appl. Meteorol.*, 43, 1083–1094.

Li, J., W. P. Menzel, W. Zhang, F. Sun, T. J. Schmit, J. J. Gurka, and E. Weisz (2004b), Synergistic use of MODIS and AIRS in a variational retrieval of cloud parameters, *J. Appl. Meteorol.*, 43, 1619–1634.

Liou, K. N. (2002), *An Introduction to Atmospheric Radiation*, 2nd ed., 583 pp., Elsevier, New York.

Liou, K. N., and S.-C. Ou (1979), Infrared radiative transfer in finite cloud layers, *J. Atmos. Sci.*, 36, 1985–1996.

Menzel, W. P., B. A. Baum, K. I. Strabala, and R. A. Frey (2002), Cloud top properties and cloud phase algorithm theoretical basis document, in *ATBD-MOD-04*, Version 6.0, 62 pp., NASA, Greenbelt, MD. (http://modis.gsfc.nasa.gov/atbd/atbd_mod04.pdf)

Nasiri, S. L., and B. A. Baum (2004), Daytime multilayered cloud detection using multispectral imager data, *J. Atmos. Oceanic Technol.*, 21, 1145–1155.

Nasiri, S. L., and B. H. Kahn (2006), Infrared cloud phase determination from MODIS and AIRS, paper presented at 14th Conference on Satellite Meteorology and Oceanography, Atlanta, Georgia, January 29–February 2.

Olsen, E.T., E. Fetzer, S.-Y. Lee, E. Manning, J. Blaisdell, and J. Susskind (2005), AIRS/AMSU/HSB Version 4.0 Level 2 QA Quick Start, 11 pp., NASA, Pasadena, CA. (http://daac.gsfc.nasa.gov/AIRS/documentation/v4_docs/v4_docs_list.shtml)

Pierangelo, C., M. Mishchenko, Y. Balkanski, and A. Chédin (2005), Retrieving the effective radius of Saharan dust coarse mode from AIRS, *Geophys. Res. Lett.*, 32, L20813, doi:10.1029/2005GL023425.

Platnick, S., M. D. King, S. A. Ackerman, W. P. Menzel, B. A. Baum, J. C. Riédi, and R. A. Frey (2003), The MODIS cloud products: Algorithms and examples from Terra, *IEEE Trans. Geosci. Remote Sens.*, 41, 459–473.

Rossow, W. B. (1989), Measuring cloud properties from space: A review, *J. Clim.*, 2, 201–213.

Rossow, W. B., et al. (1985), ISCCP cloud algorithm intercomparisons, *J. Clim. Appl. Meteorol.*, 24, 877–903.

Rossow, W. B., A. W. Walker, and L. C. Garder (1993), Comparison of ISCCP and other cloud amounts, *J. Clim.*, *6*, 2394–2418.

Stephens, G. L. (2005), Cloud feedbacks in the climate system: A critical review, *J. Clim.*, *18*, 237–273.

Stephens, G. L., et al. (2002), The CloudSat mission and the A-train, *Bull. Am. Meteorol. Soc.*, *83*, 1771–1790.

Susskind, J., C. D. Barnett, and J. M. Blaisdell (2003), Retrieval of atmospheric and surface parameters from AIRS/AMSU/HSB data in the presence of clouds, *IEEE Trans. Geosci. Remote Sens.*, *41*, 390–409.

Susskind, J., C. Barnet, J. Blaisdell, L. Iredell, F. Keita, L. Kouvaris, G. Molnar, and M. Chahine (2006), Accuracy of geophysical parameters derived from Atmospheric Infrared Sounder/Advanced Microwave Sounding Unit as a function of fractional cloud cover, *J. Geophys. Res.*, *111*, D09S17, doi:10.1029/2005JD006272.

Thomas, S. M., A. K. Heidinger, and M. J. Pavolonis (2004), Comparison of NOAA's operational AVHRR-derived cloud amount to other satellite-derived cloud climatologies, *J. Clim.*, *17*, 4805–4822.

Tobin, D. C., H. E. Revercomb, C. C. Moeller, and T. S. Pagano (2006), Use of AIRS high spectral resolution spectra to assess the calibration of MODIS on EOS Aqua, *J. Geophys. Res.*, *111*, D09S05, doi:10.1029/2005JD006095.

Wei, H., P. Yang, J. Li, B. A. Baum, H.-L. Huang, S. Platnick, Y. Hu, and L. Strow (2004), Retrieval of semitransparent ice cloud optical thickness from Atmospheric Infrared Sounder (AIRS) measurements, *IEEE Trans. Geosci. Remote Sens.*, *42*, 2254–2267.

Wielicki, B. A., and J. A. Coakley Jr. (1981), Cloud retrieval using infrared sounder data: Error analysis, *J. Appl. Meteorol.*, *20*, 157–169.

Wielicki, B. A., and L. Parker (1992), On the determination of cloud cover from satellite sensors: The effect of sensor spatial resolution, *J. Geophys. Res.*, *97*, 12,799–12,823.

Winker, D. M., J. Pelon, and M. P. McCormick (2003), The CALIPSO mission: Spaceborne lidar for observation of aerosols and clouds, in Lidar Remote Sensing for Industry and Environment Monitoring III, vol. *4893*, SPIE, Bellingham, WA.

Yue, Q., K. N. Liou, S. C. Ou, B. H. Kahn, P. Yang, and G. G. Mace (2007), Interpretation of AIRS data in thin cirrus atmospheres based on a fast radiative transfer model, *J. Atmos. Sci.*, in press.

_____

A. Eldering, E. J. Fetzer, E. Fishbein, M. J. Garay, B. H. Kahn, and S.-Y. Lee, Jet Propulsion Laboratory, 4800 Oak Grove Drive, Mail Stop 169-237, Pasadena, CA 91109, USA. (brian.h.kahn@jpl.nasa.gov)

S. L. Nasiri, Department of Atmospheric Sciences, Texas A&M University, College Station, TX, USA.